Alternative stable conformation capable of protein misinteraction links tRNA synthetase to peripheral neuropathy

David Blocquel[1], Sheng Li[2], Na Wei[1], Herwin Daub[3], Mathew Sajish[1], Maria-Luise Erfurth[4], Grace Kooi[1], Jiadong Zhou[1], Ge Bai[1], Paul Schimmel[1,5], Albena Jordanova[4] and Xiang-Lei Yang[1,*]

[1]Department of Molecular Medicine, The Scripps Research Institute, La Jolla, CA 92037, USA, [2]Department of Medicine, University of California, San Diego, La Jolla, CA 92037, USA, [3]Dynamic Biosensors GmbH, 82152 Martinsried, Germany, [4]Molecular Neurogenomics Group, VIB Center for Molecular Neurology, University of Antwerp, 2610 Antwerpen, Belgium and [5]The Skaggs Institute for Chemical Biology, The Scripps Research Institute, La Jolla, CA 92037, USA

ABSTRACT

While having multiple aminoacyl-tRNA synthetases implicated in Charcot-Marie-Tooth (CMT) disease suggests a common mechanism, a defect in enzymatic activity is not shared among the CMT-causing mutants. Protein misfolding is a common hypothesis underlying the development of many neurological diseases. Its process usually involves an initial reduction in protein stability and then the subsequent oligomerization and aggregation. Here, we study the structural effect of three CMT-causing mutations in tyrosyl-tRNA synthetase (TyrRS or *YARS*). Through various approaches, we found that the mutations do not induce changes in protein secondary structures, or shared effects on oligomerization state and stability. However, all mutations provide access to a surface masked in the wild-type enzyme, and that access correlates with protein misinteraction. With recent data on another CMT-linked tRNA synthetase, we suggest that an inherent plasticity, engendering the formation of alternative stable conformations capable of aberrant interactions, links the tRNA synthetase family to CMT.

INTRODUCTION

Charcot-Marie-Tooth disease (CMT) is one of the most common inherited neurological disorders, affecting 2.8 million people worldwide of all races and ethnic groups (1). Having no effective therapies, the disease causes degeneration of the peripheral nerves and results in a loss of muscle tissue and sensation in hands and feet. Despite similar clinical presentations, CMT is associated with vast genetic heterogeneity: so far, mutations in more than 90 genes are causatively linked to the disease (2). Among them, six encode aminoacyl-tRNA synthetases (i.e., glycyl-(3), tyrosyl-(4), alanyl-(5), histidyl-(6), lysyl-(7) and methionyl-(8)-tRNA synthetase [GlyRS or *GARS*, TyrRS or *YARS*, AlaRS *or AARS*, HisRS *or HARS*, LysRS *or KARS*, and MetRS *or MARS*]), and represent the largest gene family implicated in CMT.

Aminoacyl-tRNA synthetases catalyze an essential reaction for translation. Each of the 20 proteinogenic amino acids encoded by the universal genetic code has its own tRNA synthetase. The aminoacylation reaction links amino acids to the 3′-ends of their cognate tRNAs in two-steps: first, an amino acid (aa) is activated by ATP to generate aa-AMP; second, the aminoacyl moiety is transferred from aa-AMP to the 3′ end of the cognate tRNA to generate aa-tRNA (9,10) (Supplementary Figure S1). Importantly, it is the tRNA synthetase-catalyzed aminoacylation reaction that establishes the rules of the genetic code by pairing each amino acid with a tRNA harboring the cognate anticodon trinucleotide. Therefore, the tRNA synthetase family is considered to be one of the most ancient and essential protein families (11). Additionally, during the evolution of biological complexity, tRNA synthetases have developed a broad range of regulatory functions beyond their classic enzymatic role in translation (12–17).

The involvement of multiple members of the same family suggests a common mechanism, yet defect in tRNA aminoacylation is not shared among the CMT-causing mutants of tRNA synthetases. For example, the E71G mutant of GlyRS (GlyRS^{E71G}) and E196K mutant of TyrRS (TyrRS^{E196K}) are strongly associated with CMT type 2D (CMT2D) (3) and dominant intermediate CMT type C

*To whom correspondence should be addressed. Tel: +1 858 784 8976; Fax: +1 858 784 8990; Email: xlyang@scripps.edu

(DI-CMTC) [4], respectively, and both have wild-type-like aminoacylation activities [18,19]. In previous work, we studied several CMT2D mutants (GlyRS[CMT2D]) and revealed that they all show similar conformational opening compared with the wild-type GlyRS [20]. We also found that GlyRS[CMT2D] proteins, including GlyRS[E71G], gain aberrant interaction with neuropilin-1 (Nrp1) [21]. The aberrant interaction competitively interferes with the binding of the cognate ligand vascular endothelial growth factor (VEGF) to Nrp1, thereby disrupting the neurotropic effect of VEGF-Nrp1 signaling and contributing to the neurodegeneration [21].

While GlyRS is a class II tRNA synthetase, whose catalytic domain is composed of an anti-parallel β-sheet flanked by α-helices, TyrRS is a class I tRNA synthetase with a characteristic Rossmann fold composed of mostly parallel β-strands connected by α-helices as the catalytic domain. So far, five mutations in the *YARS* gene have been linked to DI-CMTC, characterized by intermediately reduced nerve conduction velocities, axonal degeneration, and mild demyelination [4,22,23]. All mutations are dominants, with one mutated and one wild-type allele found in each DI-CMTC patient. Among them, three mutants have been enzymatically characterized, including two missense mutations (G41R and E196K) and a 12-bp in-frame deletion that results in the deletion of four amino acids (Δ153-156VKQV) [19,24]. Also, the pathogenicity of these three mutants have been recapitulated in transgenic *Drosophila* models [19]. Indeed, flies expressing the enzymatically intact TyrRS[E196K] mutant display comparable or, in some assays, more pronounced features of neurodegeneration than flies expressing the aminoacylation compromised TyrRS mutants (i.e. TyrRS[G41R] and TyrRS[Δ153-156]) [19]. These and other studies suggested that the DI-CMTC phenotype, like CMT2D, is due to toxic gain-of-function that could be shared by all mutants [19,25]. However, the nature of the gain-of-function remains elusive. Specifically, does the gain-of-function of DI-CMTC mutants also link to conformational opening and a capacity for making aberrant interactions?

We set out to investigate the biochemical, biophysical, and structural properties of the three TyrRS mutants. We found that DI-CMTC mutations minimally affect the content of secondary structures and do not share effects on protein stability. However, we revealed a conformational change induced by each of the two missense mutations (G41R and E196K). Although the deletion mutation (Δ153–156) does not induce the conformational change, all three mutants make the same aberrant protein-protein interaction. This and other evidences suggest that deletion of 153–156 residues exposes the same area that is opened by G41R and E196K mutations. Thus, all DI-CMTC mutations, like CMT2D mutations, cause structural opening to expose a new surface for potential pathological interactions.

MATERIALS AND METHODS

Construction of expression plasmids

The full-length TyrRS and CMT mutants constructs, encoding residues 1–528, with a hexahistidine tag fused to their C-termini, have been obtained by PCR using the PfuUltra II polymerase and cloned into the pET-20b vector. To generate the mini-TyrRS and mini-CMT mutants, the region coding for aa 1–364 were amplified with the addition of a C-terminal His-Tag by PCR and cloned in the same way into the pET-20b vector.

The full-length ORFs were also amplified by PCR and cloned into the PGEX-6P-1 in order to generate GST-TyrRS and GST-CMT mutants fusion proteins that were used for Biolayer Interferometry experiments.

The expression plasmid for RBCC was obtained by cloning by PCR the region coding for the residues 65–378 of TRIM28 into a pET-20b vector containing a hexahistidine tag in the N-terminus.

Expression and purification of TyrRS, DI-CMTC mutants, RBCC and GST-fusion proteins

The *Escherichia coli* strains Rosetta [DE3] pLysS (Novagen) was used for expression of TyrRS, mini-TyrRS, GST-fusion proteins and RBCC recombinant proteins. Cultures were grown overnight to saturation in LB medium containing 100 μg/ml ampicilin and 34 μg/ml chloramphenicol. An aliquot of the overnight culture was diluted 1/25 in SB medium and grown at 37°C. At OD_{600} of 0.7, isopropyl ß-D-thiogalactopyranoside (IPTG) was added to a final concentration of 0.2 mM, and the cells were grown at 37°C for 3 h. The induced cells were harvested, washed and collected by centrifugation (5000 g, 10 min). The resulting bacterial pellets were frozen at –20°C.

The pellet was resuspended in 5 volumes (v/w) buffer A (50 mM Tris–HCl pH 8, 300 mM NaCl, 20 mM imidazole, 1 mM phenyl-methyl-sulphonyl-fluoride (PMSF) supplemented with lysozyme 0.1 mg/ml, DNAse I 10 μg/ml (Zymo Research), 20 mM $MgSO_4$ and protease inhibitor cocktail (Sigma) (50 μl/g cells). After a 20 min incubation with gentle agitation, the cells were disrupted by sonication (using a 750 W sonicator and 5 cycles of 30 s each at 60% power output). The lysate was clarified by centrifugation at 35 000 g for 30 min. Starting from a 1 l culture, the clarified supernatant was injected onto a 5-ml HisTrap FF column (GE Healthcare), previously equilibrated in buffer A supplemented with 1 M NaCl. Elution was carried out using a gradient of imidazole in buffer A supplemented with 1 M NaCl. The fractions containing the protein were combined and loaded onto a Superdex 200 HR 16/60 column (GE Healthcare) and eluted in either 10 mM Tris–HCl, 300 mM NaCl, 1 mM Tris(2-carboxyethyl)phosphine (TCEP), pH 7.5. The protein was concentrated using Centricon Plus-20 (molecular cutoff of 3000 Da) (Millipore) and then stored at –20°C.

For the GST-fusion proteins, a GSTrap column was used instead of HisTrap and the protein was eluted using a buffer containing 50 mM Tris and 10 mM of reduced glutathione at pH 8. The elution was loaded onto a Superdex 200 and eluted in a final buffer composed of 10 mM Tris–HCl, 300 mM NaCl, 1 mM TCEP at pH 7.5.

All purification steps, except for gel filtrations, were carried out at 4°C. Apparent molecular mass of proteins eluted from the gel filtration column was deduced from a calibration carried out with low molecular weight and high

molecular weight calibration kits (Amersham Pharmacia Biotech). Protein concentrations were calculated using the theoretical absorption coefficients ε (mg/ml.cm) at 280 nm as obtained using the program ProtParam at the EXPASY server (http://www.expasy.ch/tools).

Far-UV circular dichroism (CD)

Spectra were recorded on a AVIV Model400 dichrograph using 1-mm quartz cells in 10 mM sodium phosphate pH 7 at 20°C. CD spectra were measured between 185 and 260 nm, at 0.2 nm/min and were averaged from three independent acquisitions. Mean molar ellipticity values per residue (MRE) were calculated as MRE = $3300m \Delta A/(l\,c\,n)$, where l (path length) = 0.1 cm, n (number of residues) = 79, m (molecular mass in daltons) = 9040 and c (protein concentration in mg/ml) = 0.1. Spectra were deconvoluted using the DICHROWEB website (http://dichroweb.cryst.bbk.ac.uk/html/home.shtml) which was supported by grants to the BBSRC Center for Protein and Membrane Structure and Dynamics (CPMSD) [26]. The CDSSTR deconvolution method was used to estimate the α-helical content using the reference protein set 7.

Thermal shift assays (TSA)

Thermal shifts assays were performed on a StepOnePlus 96 Real Time Cycler (Applied Biosystems). The dye from the 'Protein Thermal Shift™ Kit' (ThermoFisher Scientific) was used to monitor the thermal stability of protein by binding to the exposed hydrophobic residues. Solutions of 5 μl of protein thermal shift buffer, 2.5 μl of diluted thermal shift dye (8×) and 12.5 μl of protein at 0.5 mg/ml (with or without 2 mM tyrosine) were added to the wells of a 96-well Optical Reaction Plates (Applied Biosystems). (To increase the solubility of tyrosine, the buffer was preheated to 50°C before adding the amino acid.) The plates were sealed with optical sealing tape (Bio-Rad) and heated with the RT-PCR from 20 to 90°C in increments of 0.5°C. Measurements were done in triplicate and analysed with the corresponding Protein Thermal Shift™ Software (ThermoFisher Scientific).

Quantification of the monomer–dimer equilibrium

Each protein sample (200 μl) was injected onto a Superdex 200 chromatography column (GE Healthcare, 10/300GL) in PBS buffer (NaCl 137 mM, PO_4^{3-} 10 mM, KCl 2.7 mM) at pH 7.5 containing 5 mM β-mercaptoethanol and protein absorbance at 280 nm was monitored. The column was calibrated using standard proteins. To estimate the apparent monomer–dimer equilibrium dissociation constants of each protein (ranging from 100 nM to 30 μM), 200 μl were loaded onto a Superdex 200 chromatography column. The elution volume peak of each concentration was monitored by its absorbance at 280 nm. Due to undetectable absorbance of the proteins at low concentrations, 0.5 ml fractions from elution volume ranges of 12 ml to 16 ml were collected and then subjected to SDS-PAGE and immunoblotted with anti-TyrRS antibodies to identify the elution volume peak at each concentration. Elution volume shift was defined as the fractional distance between the monomer and

dimer peaks. This difference was plotted versus concentration. The apparent K_d was taken as the concentration at which the volume shift is half-way between the monomer and dimer peaks.

Crystal structure analysis

Crystallization experiments were performed immediately after protein purification. Screening experiments were carried out using the sitting-drop vapor diffusion method at 20°C in 96-well MRC crystallization plates using a nanodrop-dispensing robot (TTP Labtech's mosquito® Crystal) and various commercial crystallization kits (Molecular Dimensions Limited, Emerald BioStructures and GenaBiosciences). Reservoir solutions were 30 μl in volume and crystallization drops were composed of 100, 200 or 300 nl protein solution at 10 mg/ml and 100 nl of reservoir solution. Crystallization plates were sealed with transparent film after set-up of the drops and transferred to a storage cabinet at 20°C.

Mini-TyrRS[G41R] crystals grew typically within 48 h to a size of 0.1 × 0.1 × 0.05 mm³ by mixing 300 nl protein at 10 mg/ml with 100 nl of the same condition used for Mini-TyrRS[WT] crystals [27]. Mini-TyrRS[E196K] crystals grew within 3 days to a size of 0.2 × 0.1 × 0.05 mm³ by mixing 300 nl of protein at 10 mg/ml with 100 nl of the same solution. Single crystals were harvested from the drop and flash frozen in liquid nitrogen at 100 K with 2-methyl-2,4-pentanediol (MPD) as cryo-protectant. Diffraction data sets were collected at the Stanford Synchrotron Radiation Lightsource (SSRL).

Small-angle X-ray scattering (SAXS) and *ab initio* shape reconstruction

All SAXS measurements were carried out at the SSRL on beamline BL4-2 at a working energy of 12.5 keV corresponding to λ = 0.992 Å. The sample-to-detector distance of the X-rays was 2.847 m, leading to scattering vectors q ranging from 0.028 to 4.525 nm⁻¹. The scattering vector is defined as $q = 4\pi/\lambda \sin\theta$, where 2θ is the scattering angle. The exposure time was optimized to reduce radiation damage. Data reduction was performed using the established procedure available at the beamline, and buffer background runs were subtracted from sample runs. The radius of gyration (R_g) and forward intensity at zero angle $I(0)$ were determined with the program PRIMUS [28] according to the Guinier approximation at low values, in a $Q.R_g$ range up to 1.3 [29]:

$$\text{Ln}\,[I(Q)] = \text{Ln}\,[I_0] - \frac{Q^2 R_g^2}{3}$$

Q: the scattering vector; $I(Q)$: the intensity as a function of the magnitude of the scattering vector; I_0: intensity at zero angle; R_g: radius of gyration of the molecule.

The forward scattering intensity was calibrated using bovine serum albumin as reference. The R_g and pairwise distance distribution function, $P(r)$, were calculated with the program GNOM. The maximum dimension (D_{max}) value was adjusted such that the R_g value obtained from GNOM agreed with that obtained from the Guinier analysis.

SAXS data were collected at 10°C using 30 µl of five different protein concentrations ranging from 0.5 to 10 mg/ml in 10 mM Tris–HCl (pH 8.5) buffer with 5 mM EDTA, and loaded in a fully automated sample charger. Ten exposures each of 10 s were made for each protein concentration and were combined to give the average scattering curve for each measurement. Any data points affected by aggregation, possibly induced by radiation damages were excluded. The profiles obtained at five different protein concentrations had the same shape and were flat at low q values indicating the absence of significant aggregation. Then, we used the higher concentration to have the maximum information at high resolution.

Three-dimensional bead models were built by fitting the scattering data with the program DAMMIF (30). Thirty independents models were generated with DAMMIF assuming P2 symmetry. The models resulting from independent runs were superimposed using the DAMAVER suite (31). This yielded an initial alignment of structures based on their axes of inertia followed by minimization of the normalized spatial discrepancy (NSD), which is zero for identical objects and larger than one for systematically different objects. The aligned structures were then average, giving an effective occupancy to each voxel in the model, and filtered at half-maximal occupancy to produce models of the appropriate volume that were used for all subsequent analyses.

Hydrogen–deuterium exchange analysis

Before carrying out hydrogen-deuterium exchange experiments, the optimal proteolysis conditions that produced the best sequence coverage map of wild-type TyrRS were established as described (32). Briefly, 3 µl of TyrRS^{WT} protein (1mg/ml) was incubated with 18 µl of 0.08 M GuHCl and digested on immobilized pepsin column for 40 s, it was found to generate the most peptides (302) which covered 100% of WT protein sequence. To initiated H/D exchange (HDX) reactions, 3 µl of protein stock solution (WT or mutants) was mixed with 9 µl of D$_2$O buffer (8.3 mM Tris, 50 mM NaCl in D$_2$O, pH 7.6) and incubated for 10, 100, 1000, 10 000 and 100 000 s at 0°C. At the designated times, HDX reaction was quenched by adding 18 µl of ice old quench buffer (0.08 M GuHCl, 0.8% formic acid, 16.6% glycerol) and samples were immediately frozen at –80°C. In addition, non-deuterated and fully deuterated samples were also prepared as previously described (33). The 30 µl quenched samples were thawed at 4°C and immediately passed over the immobilized pepsin column (1 × 20 mm, 40 mg/ml porcine pepsin (Sigma)). The digested peptides were collected on a trap column (Michrom MAGIC C18AQ, 0.2 × 2 mm) for desalting and separated with a Magic C18 column (Michrom, 0.2 × 50 mm, 3 µm, 200 Å) by a 30 min linear acetonitrile gradient of 6.4–38.4%. The accurate peptide mass measurement was performed with an OrbiTrap Elite mass spectrometer (Thermo Fisher Scientific), which was setup for optimal HDX performance with minimum back-exchange rate (34,35). Data acquisition was completed in either data-dependent MS/MS or MS1 profile mode and peptide identification was done using Proteom Discoverer software (Thermo Fisher Scientific). Deuterium incorporation levels of each peptide at each time-points were determined

by HDXaminer (Sierra Analytics Inc) with back-exchange correction use above control samples (36).

SwitchSense analysis

Sample preparation. Forty microgram of thiol-modified DNA (5′-ATC AGC GTT CGA TGC TTC CGA CTA ATC AGC CAT ATC AGC TTA CGA CTA-(SH-modifier)-3′ was activated with heterobifunctional crosslinker sulfosuccinimidyl 4-(*N*-maleimidomethyl)cyclohexane-1-carboxylate (Sulfo-SMCC) in PBS for 20 min. In a second reaction, the activated DNA was covalently linked (using an amine coupling strategy) via either the ε-amino groups of reactive lysines or the N-terminal α-amino group of the Tyrosyl–tRNA synthetase constructs. The Tyrosyl–tRNA synthetase–DNA conjugation reaction mixtures were incubated at 4°C for 12 h and subsequently purified on an anion-exchange column (YMC-BioPro QA).

Single-stranded DNA oligonucleotides (48 bp) are tethered to a gold microelectrode by thiol chemistry. Tethered strands have the following sequence: 5′-(SH-modifier)-TAG TCG TAA GCT GAT ATG GCT GAT TAG TCG AAA GCA TCG AAC GCT GAT-(fluorophore)-3′. The Tyrosyl–tRNA synthetase conjugates are hybridized to their complementary tethered DNA nanolevers, thus immobilizing the Tyrosyl-tRNA on the biosensor surface.

Sample measurement. The Tyrosyl–tRNA synthetase-DNA conjugates were immobilized onto the biosensor surface (by hybridization) at a concentration of 200 nM. The experimental running buffer used was PE40 (10 mM, Na$_2$HPO$_4$/ NaH$_2$PO$_4$, 40 mM NaCl, 0.05% Tween20). For the determination of hydrodynamic drag in solution, a reporter fluorophore (probe a rhodamine-derivative with an emission maximum at 576 nm) was attached to the DNA's distal end, and read out by an epifluorescence setup. By distant-dependent, non-radiative energy transfer from reporter fluorophores to the metal surface, the DNA levers' orientation and movement can be accurately monitored. By alternating the applied surface potentials of –400 mV and +400 mV at a frequency of 10 kHz, the DNA's intrinsic negative charge enables forced switching movement of the nanolevers. Whenever a sufficiently negative potential is applied, the DNA is repelled from the surface to a standing position (Figure 5A). Conversely, positive potentials attract the DNA to the surface, transitioning the nanolever from a standing to a lying position. The nanolever movement happens on the microsecond scale, and can be fully resolved employing time-correlated single photon counting, with sampling events of 25 ns precision (37). To describe the DNA's motion between lying and standing states, the orientation of reporter fluorophores were recorded as a function of time, the fluorescence response curves. The slope and form of the sigmoidal transition within the response curve is affected by the hydrodynamic drag of the nanolevers. As such, a nanolever carrying a protein cargo at its distal end experience a notably larger hydrodynamic drag, corresponding to the hydrodynamic radius of the sampled protein. The calculation of hydrodynamic radii from these fluorescence response curves is done according to previous work (37).

Biolayer interferometry

The dissociation constants (K_d) between RBCC (aa 65–378 of TRIM28) and TyrRS or CMT mutants were obtained through biolayer interferometry with an Octet QK system (FortéBio). Samples or buffer were dispensed into 96-well plates (Greiner Bio-one) at 200 μl per well. The operating temperature was maintained at 20°C. The GST fused wt TyrRS and CMT mutants proteins were diluted into kinetic buffer (PBS with 0.1% BSA and 0.002% Tween-20) and immobilized on anti-GST sensor tips. The RBCC protein used for injections was diluted with the same buffer into a range of different concentrations.

Sensors were subsequently incubated with GST fusion protein for 5 min, until signals plateaued and immediately followed by a 2 min wash with the binding buffer to remove the unbound GST fusion protein and to serve as a baseline for the association and dissociation steps. To monitor the association, 5 μM of Tag free RBCC was added to the reaction wells for 6.5 min. To monitor protein dissociation, sensors were advanced to wells containing assay buffer for 10 min.

The equilibrium binding magnitude was defined as the net signal after reactions had plateaued and this net signal at each time point was plotted. The raw data were processed by subtraction of values for reference cells and then aligned with the association phase (0.2–0.4 s). The dissociation constants K_d were obtained by fitting the processed data with the 1:1 model in Octet analysis software with $R^2 > 0.99$ and are shown as mean ± error of fit.

RESULTS

DI-CMTC mutations do not affect protein folding

The three DI-CMTC mutation-associated residues are localized in the catalytic domain of TyrRS (Figure 1A): G41 is on one of the six β-strands that make up the structural core of the Rossmann nucleotide-binding fold catalytic domain; E196 is within an α-helix (α9) that is on the periphery of the Rossmann fold and is exposed to the solvent; and the four amino acids missing in Δ153–156 are located within a flexible loop connecting two α-helixes (α7−α8) in the CP1 domain that makes contacts at the dimer interface (27) (Figure 1B). Before carrying out a structural analysis of the mutants, we performed biochemical experiments to see if the mutations can affect the solubility and/or the folding of the protein. All human proteins were overexpressed in *E. coli* and purified from the soluble fraction of the bacterial lysate with similar yield, indicating that the protein solubility is not obviously affected by the CMT mutations. In order to monitor any possible changes in the protein secondary structures, we carried out far-UV circular dichroism (CD) experiments. All recorded CD spectra indicate properly folded proteins, and deconvolution of the spectra leads to comparable amount of α-helix and β-strands among the four proteins, suggesting that the mutations do not affect protein folding (Supplementary Figure S2).

G41R and Δ153–156 increase while E196K decreases protein stability

To study the impact of the mutations on protein stability, we performed fluorescence-based thermal shift assays (TSA). This method measures the fluorescence emission upon binding of the fluorescent probe to the hydrophobic regions of the protein that become more exposed during protein thermal denaturation. In the absence of any ligand, compared with TyrRS^{WT}, an increase in the T_m (apparent melting temperature) was observed for TyrRS$^{Δ153–156}$ (+1.1°C) and TyrRS^{G41R} (+3.5°C), whereas a large decrease in the Tm was found for TyrRS^{E196K} (–7.3°C) (Figure 1C), indicating that the DI-CMTC mutations have idiosyncratic effects on protein stability. Interestingly, except for the most stable TyrRS^{G41R}, all proteins are stabilized by the addition of tyrosine to various degrees (Figure 1C). The stabilizing effect of the amino acid substrate is most pronounced for the least stable TyrRS^{E196K} (+5.3°C). However, tyrosine binding does not change the order of the four proteins in stability (TyrRS^{G41R} > TyrRS$^{Δ153–156}$ > TyrRS^{WT} > TyrRS^{E196K}).

E196K, but not G41R and Δ153–156, affects monomer–dimer equilibrium

TyrRS is known to function as a dimer to catalyze the tRNA aminoacylation reaction. Analytical size-exclusion chromatography was performed for TyrRS^{WT}, TyrRS^{G41R}, TyrRS^{E196K} and TyrRS$^{Δ153–156}$ at a high concentration (100 μM), and each showed an apparent molecular mass of 120 ± 5 kDa, consistent with a dimeric organization for all proteins (data not shown). To investigate the effect of DI-CMTC mutations on the dimerization of TyrRS, varying concentrations of the four proteins were used to estimate the apparent dissociation constant for the monomer–dimer equilibrium. The estimated K_d for TyrRS^{G41R} and TyrRS$^{Δ153–156}$ are similar to TyrRS^{WT} with values of ∼200 nM, indicating that G41R and Δ153–156 do not affect the dimerization ability of TyrRS (Figure 1D). In contrast, the apparent dissociation constant for TyrRS^{E196K} was estimated as 4.9 μM, which is 23-fold higher than that for TyrRS^{WT}. This result indicates that the E196K mutation weakens the dimer formation of TyrRS, but this effect is not shared by other DI-CMTC mutations. It is worth noting that tRNA^{Tyr} binds to TyrRS across the dimer interface (38) (Supplementary Figure S1), which would stabilize the TyrRS dimer and may explain why E196K, despite the much-reduced K_d for dimerization, does not affect tRNA aminoacylation (19).

Crystal structures of DI-CMTC mutants G41R and E196K

Human TyrRS contains three domains: catalytic domain, anticodon binding domain, and EMAP II-like domain (39) (Figure 1A). The first two domains (mini-TyrRS) are evolutionary conserved and are necessary and sufficient for the aminoacylation activity of TyrRS (40). Although there is no crystal structure for the full-length TyrRS, the structures of both mini-TyrRS and the C-terminal EMAP II-like domain have been determined separately (27,41). In order to achieve a structural understanding of the effects caused by
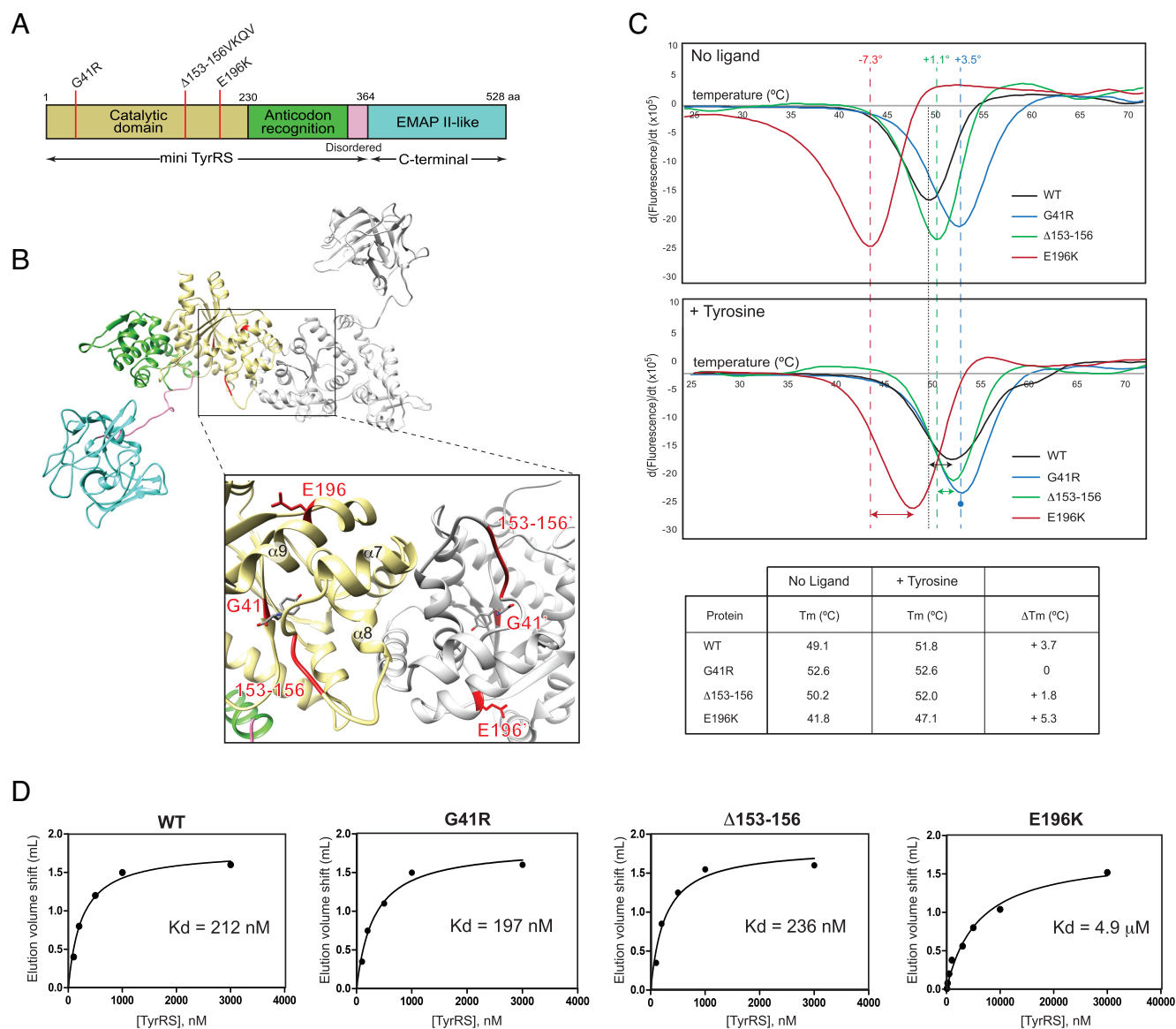
Figure 1. CMT-causing mutations on TyrRS and their effect on protein stability. (**A**) The 3 CMT-causing mutations mapped onto the domain structure of TyrRS. (**B**) Model of the full-length dimeric TyrRS structure based on the crystal structure of mini-TyrRS (pdb 1N3L) and the C-terminal EMAP II-like domain (pdb 1NTG). A close-up view at the dimer interface shows the localization of the 3 CMT mutations on each subunit. (**C**) The top panel shows the thermal shift data and the associated melting temperature (T_m) for TyrRS[WT] and the 3 CMT mutants. The middle panel shows the corresponding melting data in the presence of tyrosine (2 mM) and the arrows indicate changes in T_m from the apo form of the proteins. The table below summarizes the different melting temperatures obtained for each of the proteins with or without tyrosine, as well as the differences between the two conditions (ΔT_m). (**D**) Estimation of dimer-monomer equilibrium dissociation constant by gel filtration chromatography in combination with immunoblotting.

DI-CMTC mutations, we solved the crystal structures of mini-TyrRS[G41R] and mini-TyrRS[E196K] at 1.6 and 1.95 Å resolution, respectively.

The attempts to crystalize the full-length TyrRS[G41R] and TyrRS[E196K], as well as TyrRS[WT], have been unsuccessful, most likely due to the presence of a disordered and highly flexible linker between mini-TyrRS and EMAP II-like domain (Figure 1A and B). Interestingly, the crystal structures of both mini-TyrRS[G41R] and mini-TyrRS[E196K] are similar to that of mini-TyrRS[WT] (Figure 2A). (Compared to mini-TyrRS[WT], the root-mean-square deviation (RMSD) for 318 Cα positions is 0.27 and 0.73 Å for mini-TyrRS[G41R] and

mini-TyrRS[E196K], respectively.) The crystallization conditions used in both cases were similar to those used for mini-TyrRS[WT] (27), and the crystals have the same space group ($P2_12_12$) with each asymmetric unit containing one monomeric subunit (Supplementary Table S1).

Interestingly, in the structure of mini-TyrRS[G41R], the arginine substitution occupies the tyrosine-binding pocket (Figure 2B). This prevents tyrosine from binding to the mutant, and thus explains the lack of T_m shift in the presence of tyrosine for TyrRS[G41R] (Figure 1C) and its complete loss of aminoacylation activity (19,24). While the mini-TyrRS[G41R] structure was obtained without any ligand bind-
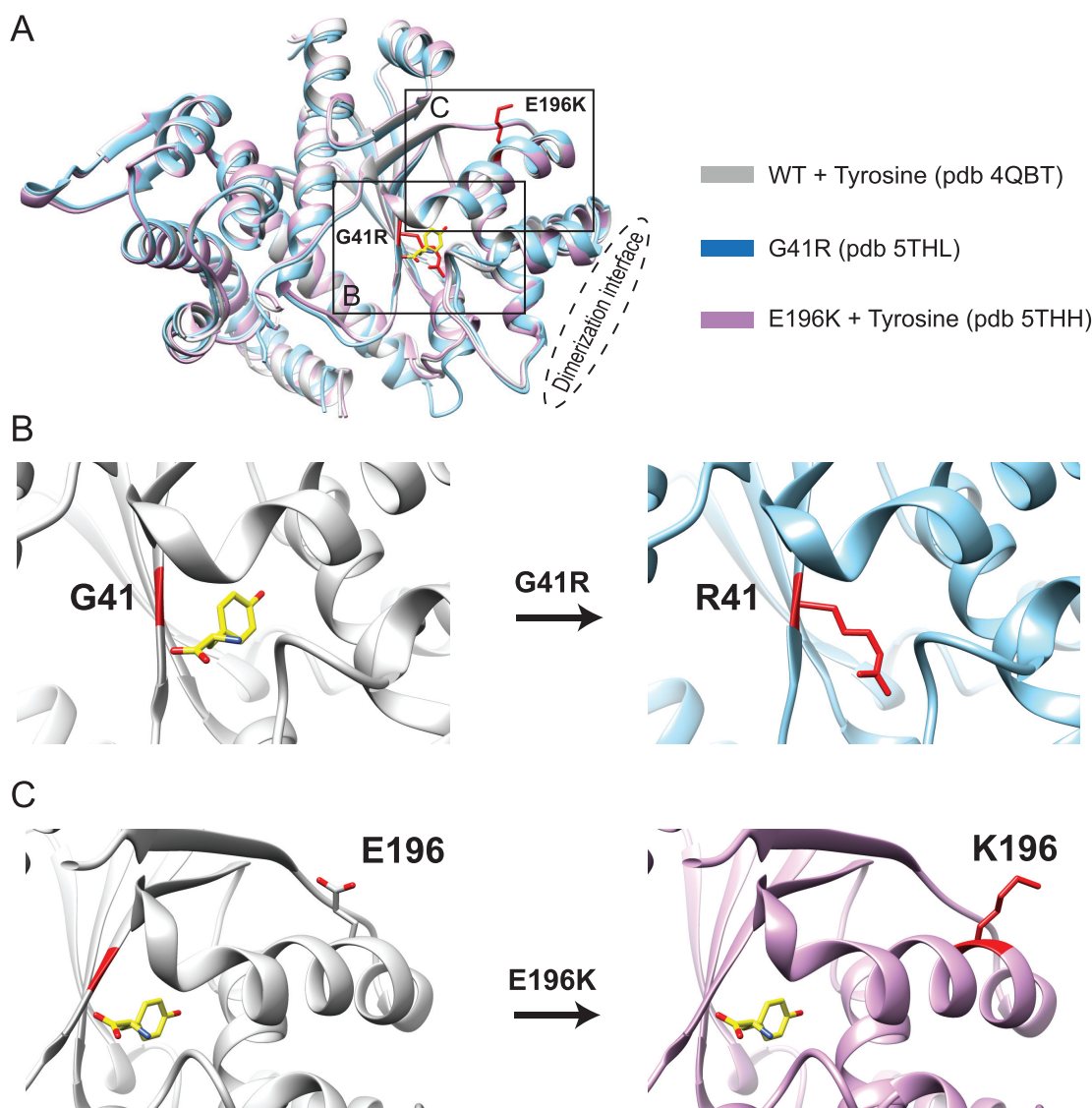
Figure 2. Crystal structures of mini-TyrRS^{G41R} and mini-TyrRS^{E196K}. (**A**) Comparison of the crystal structures of mini-TyrRS^{G41R} and mini-TyrRS^{E196K} with the co-crystal structure of mini-TyrRS^{WT}/tyrosine (pdb 4QBT). The superimposition has been made using the molecular graphics program UCSF Chimera, and the side chains of the two mutated residues (R41 and K196) are represented in red. (**B**) Close-up view of residue 41 in mini-TyrRS^{WT}/tyrosine (left panel) and mini-TyrRS^{G41R} (right panel) structures. The bound tyrosine in the active site of the mini-TyrRS^{WT} is colored in yellow and the residue 41 is colored in red. (**C**) Close-up view of residue 196 in mini-TyrRS^{WT}/tyrosine (left panel) and mini-TyrRS^{E196K} structures (right panel). The bound tyrosine in the active site of the mini-TyrRS^{WT} is colored in yellow and the residue 196 is colored in red. Note a bound tyrosine was unexpectedly found in the active site of the mini-TyrRS^{E196K} structure.

ing, all mini-TyrRS^{E196K} crystals we tested have a tyrosine bound in the active site (Figure 2C). Because no tyrosine was added to the protein during purification and crystallization, the bound tyrosine must have co-purified with mini-TyrRS^{E196K}. Because tyrosine has a strong stabilization effect on TyrRS^{E196K} (Figure 1C), it is conceivable that the tyrosine-bound form of mini-TyrRS^{E196K} is easier to crystallize than the apo form, although the apo form is the major population in solution.

We speculate the selection of a certain population during crystallization and the crystal packing forces have prevented us from capturing conformational differences between the proteins. Therefore, we started to investigate the conforma-

tions of these proteins in solution by small-angle X-ray scattering (SAXS).

SAXS reveals similar conformational change induced by G41R and E196K

SAXS experiments were performed for the full-length TyrRS^{WT} and all three DI-CMTC mutants. For each protein, the shapes of the scattering curves are independent of protein concentrations in the range of 5–185 μM. (Supplementary Figure S3A), and the corresponding Guinier plots show parallel straight lines at the very small scattering angles (the low-resolution Guinier region) (Supplementary Figure S3B), indicating the absence of significant aggrega-

tion. The molecular mass determined from the extrapolated scattering intensity at a zero angle is ranged between 111.5 and 120.7 kDa (Figure 3A), indicating dimeric organization for all proteins, consistent with the result from size-exclusion chromatography. The Guinier analysis gave R_g (radius of gyration) values of 4.62, 4.86, 4.52 and 4.89 nm for TyrRS[WT], TyrRS[G41R], TyrRS[Δ153–156] and TyrRS[E196K], respectively (Figure 3A). These values indicate an overall size increase for TyrRS[G41R] (+5.2%) and TyrRS[E196K] (+5.8%) and a size decrease for TyrRS[Δ153-156] (–2.4%), compared to TyrRS[WT].

A closer look at the scattering curves within the medium resolution region (50–25 Å) that is most sensitive to global conformational change shows a clear separation of the profiles obtained for TyrRS[WT] and TyrRS[Δ153-156] from that for TyrRS[G41R] and TyrRS[E196K] (Figure 3B). The pairwise distribution functions are also in agreement with this observation (Figure 3C), suggesting that G41R and E196K, but not Δ153-156, induce significant global conformational changes in TyrRS.

To visualize the conformational change, we carried out *ab initio* shape reconstruction from the scattering data collected at the highest concentration. For each protein, a total of 30 independent *ab initio* reconstructions were calculated and merged to generate the molecular envelop (Figure 3D). (The envelopes obtained for each protein were highly similar, as indicated by a small average normalized spatial discrepancy (NSD) value (Figure 3A). As shown in one of our previous studies (42), TyrRS[WT] forms an S-shaped molecule, with the central region containing mini-TyrRS in dimeric form and two C-terminal domains protruding toward opposite ends (Figure 3D). All three CMT mutants also display this S-shaped organization (Figure 3D; middle row); however, obvious differences were observed between TyrRS[WT] and two of the CMT mutants: TyrRS[G41R] and TyrRS[E196K]. These differences originated from the mini-TyrRS region, and caused changes in orientation of the C-terminal domains (Figure 3D; top row). The dimeric mini-TyrRS[WT] crystal structure (PDB 1N3L) fits better in the TyrRS[WT] envelope than in the TyrRS[G41R] and TyrRS[E196K] envelopes (Figure 3D). Compared to the TyrRS[WT] envelope, the central region of TyrRS[G41R] and TyrRS[E196K] envelopes bends toward the opposite direction, causing a translocation of the C-terminal domain in these two mutants (Figure 3D; bottom row). Interestingly, this translocation of the C-terminal domain and bending in the mini-TyrRS region are not observed in the TyrRS[Δ153-156] envelope, which displays the same overall conformation as TyrRS[WT] (Figure 3D).

HDX analyses confirm overall conformational opening induced by G41R and E196K

In order to pinpoint the site of the conformational change, we recorded hydrogen–deuterium exchange (HDX) for the full-length TyrRS[WT] and the three DI-CMTC mutants. HDX is a powerful analytical technique for studying protein dynamics in solution and revealing conformational changes when mutants are compared with the WT protein. After each exchange period in a D_2O buffer, the protein is rapidly proteolyzed into fragments and analyzed using high-resolution proteomics methods to gain insights on the solvent accessibility to different regions of the protein. For TyrRS[WT], the HDX-mass spectrometry analysis gave excellent peptide coverage (>90%) (Figure 4A). Interestingly, the loop region between helix α7 and α8 that flanks the four amino acids missing in TyrRS[Δ153–156] showed the most significant deuterium uptake (>80% of deuteration level after 10 s of exchange) (Figure 4A), indicating this loop is highly dynamic and exposed on the protein surface. This observation is in agreement with the fact that this region was characterized by high B-factors in the crystal structure (27,42).

Compared with TyrRS[WT], TyrRS[E196K] shows an overall increase (10.8% at 1000 s of exchange) in deuteration level. Considering that the apparent dissociation constant for the monomer–dimer equilibrium is increased for the mutant and that the protein concentration during the HDX experiment (~6 μm) is only slightly above the K_d, a larger monomer population is expected for TyrRS[E196K], which would enhance the deuterium incorporation at the dimer interface. Indeed, residues at the dimer interface (α6–α7–α8–α9 [Ser126–Gly203]) show a strong increase in deuteration levels (>40%) (Figure 4B). However, other regions of the catalytic domain outside of the dimer interface, and the majority of the anticodon binding domain also show substantial HDX increase (Figure 4B and Supplementary Figure S4A). The overall increase in deuteration level is suggestive of a more relaxed structure, consistent with the size increase observed by the SAXS analysis for TyrRS[E196K] (Figure 3A).

We also observed a slight overall increase in deuterium incorporation for TyrRS[G41R], compared with TyrRS[WT] (1.3% at 1000 s of exchange) (Figure 4C and Supplementary Figure S4B). The overall increase for TyrRS[G41R] is much smaller than that for TyrRS[E196K], and the two mutants have an opposite effect at the dimerization interface where TyrRS[G41R] shows a decrease in deuterium incorporation (Figure 4C). Because the effect of G41R on monomer-dimer equilibrium is minimal (Figure 1D), the decrease in deuterium incorporation at the dimer interface is most likely due to a stabilization effect of the R41 side chain in the active site (Figure 2B). Indeed, in the crystal structure of mini-TyrRS[G41R], the arginine side chain projects toward the dimerization interface (Figure 2A and B), and the stabilization effect of the G to R mutation has been demonstrated by the increased *Tm* for TyrRS[G41R] in the TSA experiment (Figure 1C). The stabilization effect may also contribute to the less dramatic increase in deuterium incorporation outside the dimerization interface, compared with TyrRS[E196K]. Nevertheless, the overall increase in deuterium incorporation for TyrRS[G41R] is consistent with an overall structural opening, as revealed by SAXS analysis.

As for TyrRS[Δ153–156], no significant difference from TyrRS[WT] was observed in deuterium incorporation except for slight variations around the deletion site and the dimerization interface (Figure 4D and Supplementary Figure S4C), which confirms our SAXS observation that deletion of the 4 amino acids does not induce a global conformational change.
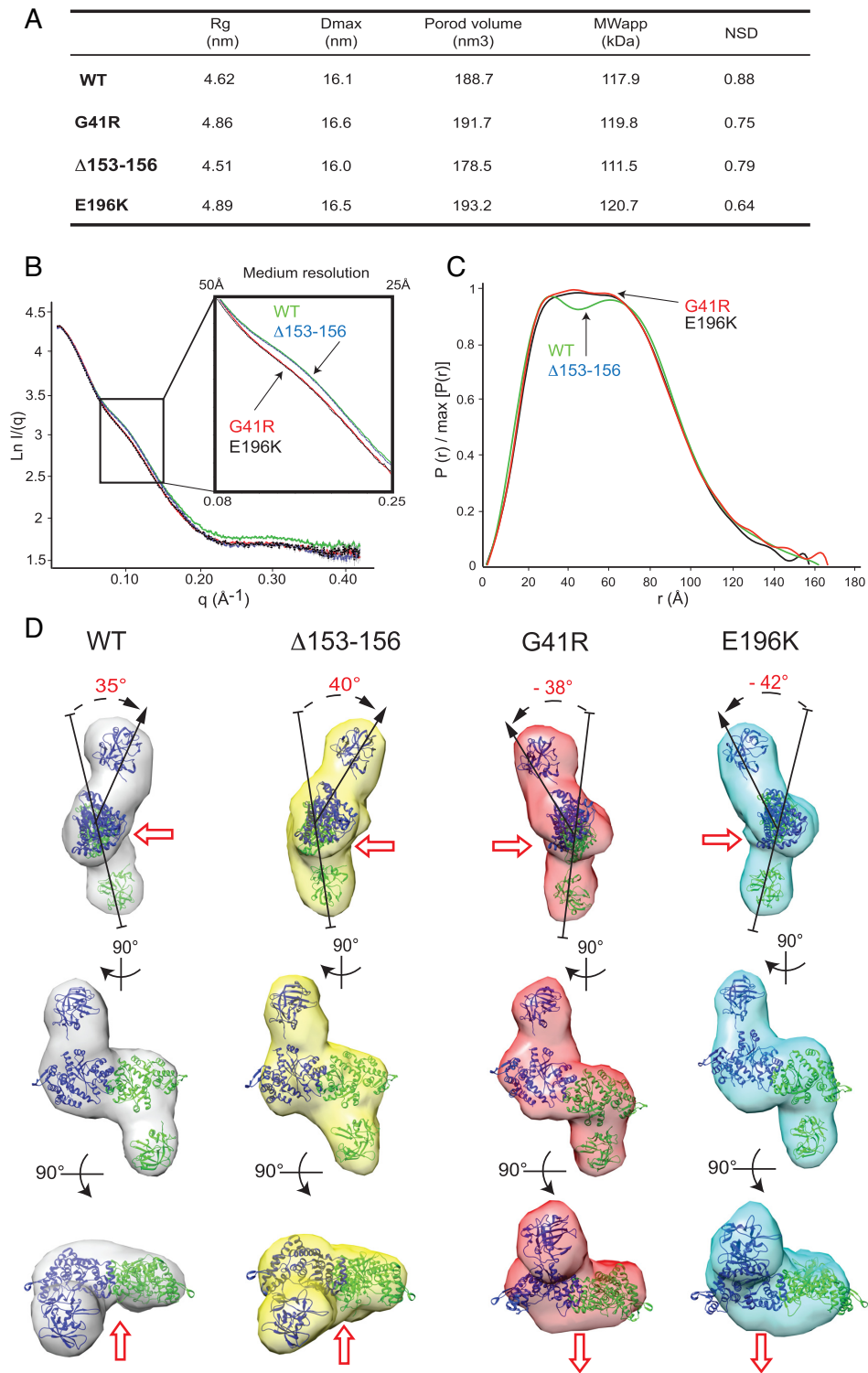
Figure 3. Small-Angle X-ray Scattering (SAXS) analysis of WT TyrRS and its CMT mutants. (**A**) Summary table of main SAXS parameters for all the proteins tested. (**B**) Experimental solution scattering data for the four proteins. The inset shows a close-up view of the medium resolution region (q values ranging from 0.08 to 0.25). (**C**) Pair distance distribution, P(r), of the SAXS data determined during data reduction with GNOM. (**D**) Three different views of the *ab initio* envelope. The structures of the dimeric mini-TyrRS and the EMAP II-like domain have been manually docked in each of the envelope. The extra densities correspond to the disorder linker, which is not present in either of the two crystal structures.
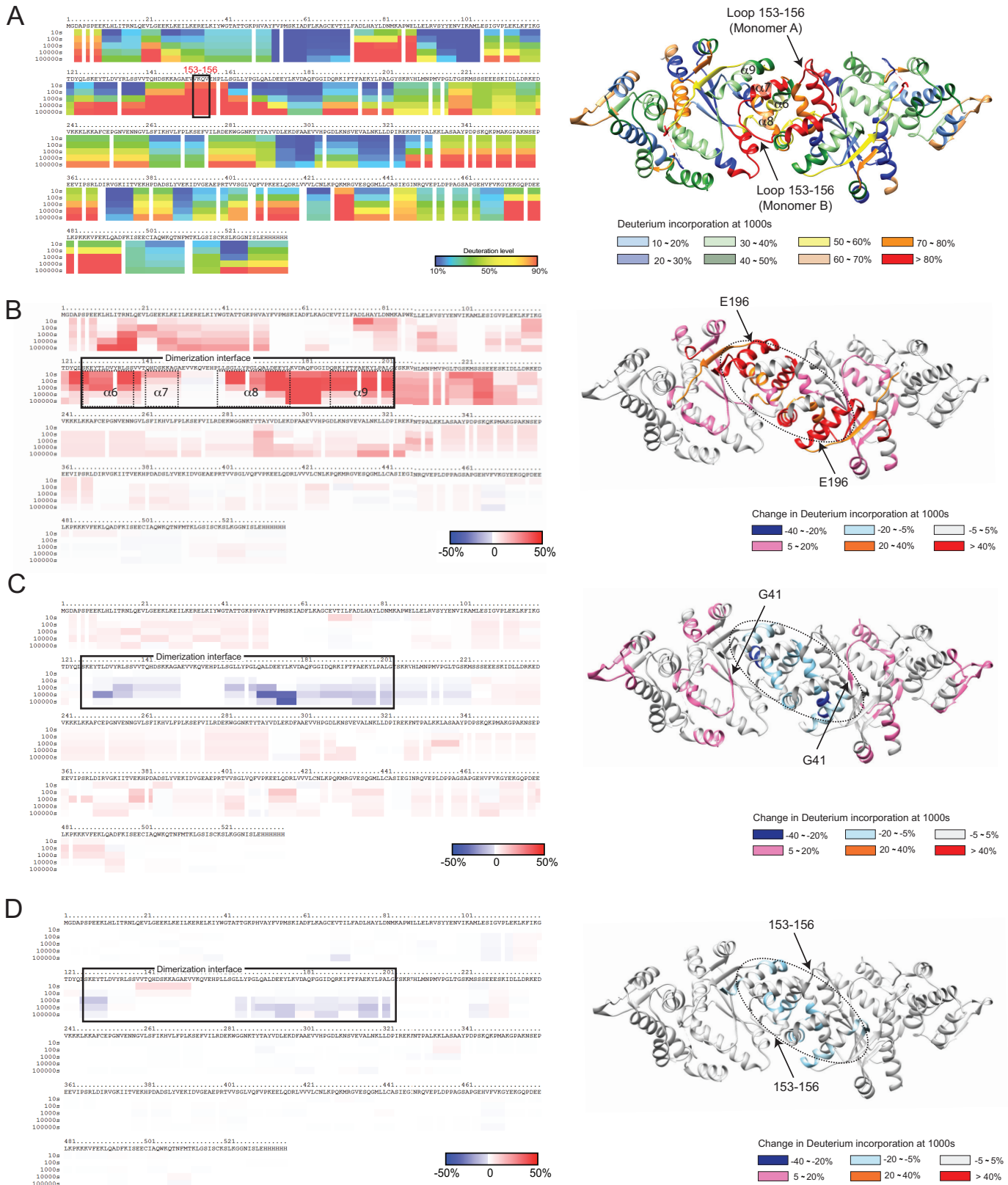
Figure 4. Hydrogen-Deuterium exchange analysis. (**A**) Left panel: raw map of deuterium incorporation for TyrRS[WT]. Right panel: mapping of the level of deuterium incorporation on the structure of the dimeric mini-TyrRS. (**B**) Difference map that shows the changes in deuterium incorporation for the E196K mutant (left panel) with a mapping of those changes on the mini-TyrRS dimer crystal structure (right panel). The three regions show most dramatic increases in deuteration level are boxed. Similar analyses have been done for the G41R (**C**) and Δ153–156 (**D**) mutants. The dotted oval in (**B**), (**C**) and (**D**) show the dimer interface.

SAXS results confirmed by hydrodynamic radii measured by switchSENSE® technology

The unique structural and dynamics properties of each mutant motivated us to further investigate them using an independent method. The switchSENSE® technology can monitor protein size in solution by assessing the hydrodynamic radius (43). The technology tethers short DNA double strands to a gold surface on one end and allows binding to proteins of interest on the other end (Figure 5A). The motion of the DNA levers is triggered by alternating the voltage across the electrode surface and is tracked in real time through a fluorescence probe attached to the DNA. Upon binding of TyrRS proteins, the hydrodynamic friction of the levers is affected and subsequently the movement of these levers. The movements were recorded (Figure 5B) and used to calculate the hydrodynamic radius of each protein (Figure 5C). To minimize the difference in dimer-monomer populations, in this experiment, we isolated the dimers by gel filtration after the conjugation with the DNA and directly subject them to the analysis. Remarkably, we found that TyrRS^{G41R} and TyrRS^{E196K} are substantially larger than TyrRS^{WT}, with a 6.9% and 10.3% increase in the hydrodynamic radius, respectively (Figure 5C). As expected, TyrRS$^{\Delta153-156}$ is smaller than TyrRS^{WT}, with an 8.63% decrease in the hydrodynamic radius. Although the changes in size as detected by the switchSENSE® technology is more pronounced than those detected by SAXS, qualitatively speaking, results from all experiments are highly consistent in suggesting G41R and E196K, but not Δ153–156, induce conformational opening in TyrRS.

All DI-CMTC mutations enhance TyrRS's ability to interact with TRIM28

Neomorphic conformational opening can lead to aberrant interactions. Although the interaction of TyrRS with tRNA seems not affected by the DI-CMTC mutations (24), protein–protein interactions may be impacted. Previously, we showed that TyrRS is trans-located from cytosol to nucleus in response to oxidative stress to protest against DNA damage (44,45). In the nucleus, TyrRS makes a direct interaction with TRIM28 to sequester this vertebrate-specific transcriptional repressor to activate the expression of DNA damage repair genes (45). The TyrRS interaction was mapped to the coiled-coil domain of TRIM28 (45). Using *E. coli*-based overexpression system, we are able to produce and purify an N-terminal fragment of TRIM28, which contains the RING, B1, B2, and the coiled-coil domain (RBCC) (Figure 6A). Although RBCC, compared with the full-length TRIM28 and the isolated coiled-coil domain, has a weaker interaction with TyrRS (45), we were able to detect the interaction using biolayer interferometry *in vitro* (Figure 6B). Remarkably, all three DI-CMTC mutants have an enhanced interaction with RBCC (Figure 6B), with a 3-fold increase for TyrRS^{G41R} and a 5-fold increase for both TyrRS^{E196K} and TyrRS$^{\Delta153-156}$ in the binding affinity.

It is remarkable to see that not only TyrRS^{E196K} and TyrRS^{G41R}, but also TyrRS$^{\Delta153-156}$ which lack conformational change, end up making the same aberrant interaction. This result suggests that residues 153–156VKQV act as a structural blocker to pr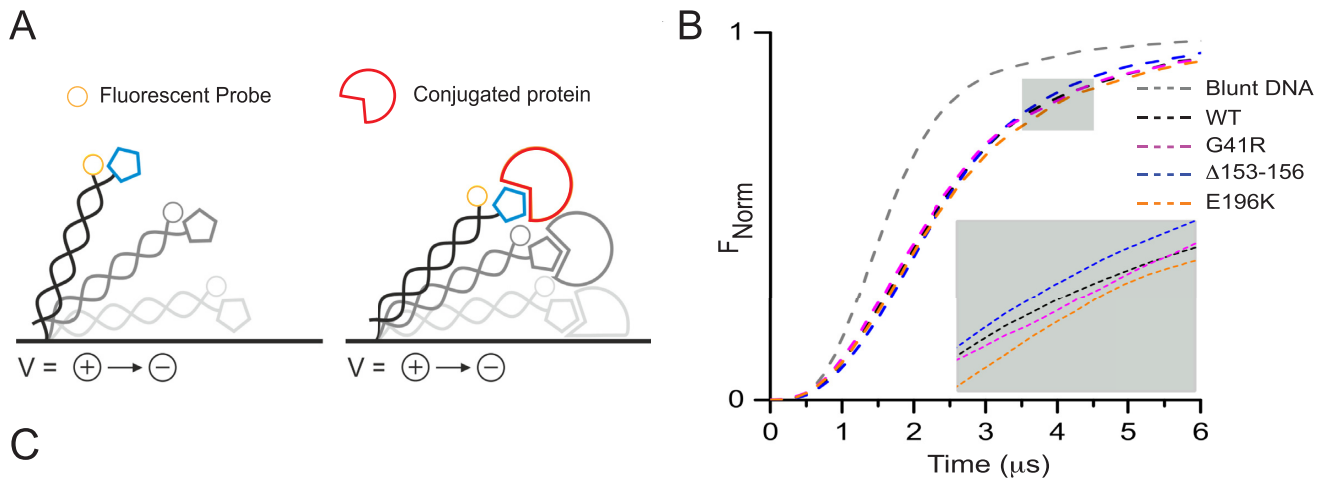event the aberrant interaction in TyrRS^{WT}. Instead of inducing a conformational opening, Δ153-156 removes the 'access blocker' to unmask a binding surface that also becomes exposed by the G41R and the E196K mutations to make the same aberrant interaction (Figure 6C). The fact that residues 153–156VKQV are located in a highly exposed and dynamic loop near the dimer interface (Figures 1B and 4A) and that removal of these residues does not cause conformational change suggest that the TRIM28 binding site is near the dimer interface (Figure 6C).

DISCUSSION

Protein misfolding is a common hypothesis underlying the development of many neurological diseases (46,47). Misfolding can expose hydrophobic residues that are normally buried within the structural core, and result in decreased protein stability and solubility. Reduced solubility is often associated with the conversion of some α-helices and unordered structures to β-strands, which further promote protein self-assembly and aggregation. The resulting aggregation eventually form amyloid-like fibrils or inclusion bodies that are commonly found in various neurological diseases such as Alzheimer's disease, Parkinson's disease, Huntington's disease, and Amyotrophic Lateral Sclerosis. However, in neurological diseases, the quantity of aggregates does not correlate with severity of clinical symptoms, suggesting that the most neurotoxic species may not be the readily detectable aggregates but rather the misfolded soluble proteins and/or small oligomers (48). Through several possible mechanisms (49), including aberrant interactions with various intracellular or extracellular targets, those misfolded soluble proteins may mediate toxic effects to disrupt cellular homeostasis and cause neuronal death. In this regard, formation of aggregates that would block the aberrant interaction may even be protective to cells.

In principle, many proteins, if not all, have the potential to misfold and form aggregates under certain conditions (47,50). This phenomenon questions whether protein misfolding is the original cause or a mediator of other causative molecular and cellular perturbations. A clear answer is not always achievable for many common neurological diseases such as the Alzheimer's and Parkinson's diseases, where the genetic makeup for the diseases is complex. However, for CMT, the causal relationship between certain mutation and the disease is clear, oftentimes with complete penetrance. For example, G41R and E196K mutations in YARS were each segregated with DI-CMTC in large families (4). Although Δ153–156 is a *de novo* mutation without family history, the pathogenicity of this mutation, as well as that of G41R and E196K, has been recapitulated in transgenic *Drosophila* models (19). Therefore, structural abnormalities, especially those shared among different disease-causing mutations, are likely to be the fundamental cause of the disease.

We have demonstrated in this study that protein instability is not a common feature of DI-CMTC mutants. E196K is the only mutation that causes a decrease in thermal stability (Figure 1C). The other two mutants (G41R and Δ153–156) are in fact more stable than the WT protein. The E196K mutation also decreases the dimerization capacity

Figure 5. SwitchSENSE® sizing analysis of WT TyrRS and its CMT mutants. (**A**) Schematic of the movement of a blunt DNA lever (left) and a DNA lever with a protein covalently attached to its distal end (right) in a switchSENSE® sizing analysis experiment. (**B**) Experimental data of fluorescence response during upward switching (mean curves of four measurements are shown) of blunt DNA (gray), TyrRS[WT] (black), TyrRS[G41R] (magenta), TyrRS[Δ153-156] (blue) and TyrRS[E196K] (orange) attached to the DNA's distal end. The grey box highlights the differences in fluorescence response (3.5–4.5 µs), which contributes to difference in hydrodynamic diameter. (**C**) Summary table of switchSENSE® sizing data. For the calculation of the hydrodynamic radius with the Theoretical Lollipop Model, the complete range of fluorescence response curves are respected (0–6 µs).

of TyrRS, but again this effect is not shared by the other two mutations (Figure 1D). All mutants have proper folding in terms of secondary structure contents (Supplementary Figure S2). However, they seem to share a similar conformational opening, either induced by a missense mutation (G41R or E196K) or enabled by a specific deletion (Δ153–156). Therefore, we suggest that DI-CMTC is not caused by loss of protein stability, but rather by a specific change in protein structure to generate an alternative stable conformation. It may not be appropriate to refer this structural change as protein misfolding. An alternative stable conformation may share some, but not all, consequences of a misfolded protein. For example, these stable alternative conformers are less likely to cause protein aggregation than are misfolded proteins.

The alternative stable conformation adopted by DI-CMTC mutants can explain the toxic gain-of-function mechanism suggested by genetic studies in *Drosophila* (19,25) and the dominant genetic trait of DI-CMTC. However, the aberrant TRIM28 interaction that we demonstrated may not be the only aberrant interaction for DI-CMTC mutants. Rather, it serves as a proof of concept that,

despite the uniqueness of each DI-CMTC mutation in affecting the biophysical and biochemical properties of the protein, all mutations share the same capacity for making an aberrant interaction, or interactions, that may uniquely, or collectively, contribute to the disease phenotypes. To further advance our understanding of the molecular mechanism of DI-CMTC, future work should be focused on determining whether the aberrant interaction with TRIM28 is linked to the pathology and to identify, if any, additional aberrant interaction partners that are common for DI-CMTC mutants. We should note that a TRIM28 ortholog is not found in *Drosophila*, suggesting that the aberrant TyrRS–TRIM28 interaction per se is not involved in the development of CMT-like phenotypes in the *Drosophila* model.

What we have revealed here for DI-CMTC mutants of TyrRS shares remarkable commonality with CMT2D mutants of GlyRS. Most CMT2D-causing mutations are also located in the catalytic domain, which also mediates the dimerization of the synthetase (45,51). The effect of CMT2D-causing mutations on dimerization is also idiosyncratic, with some promoting (e.g., G526R) while others
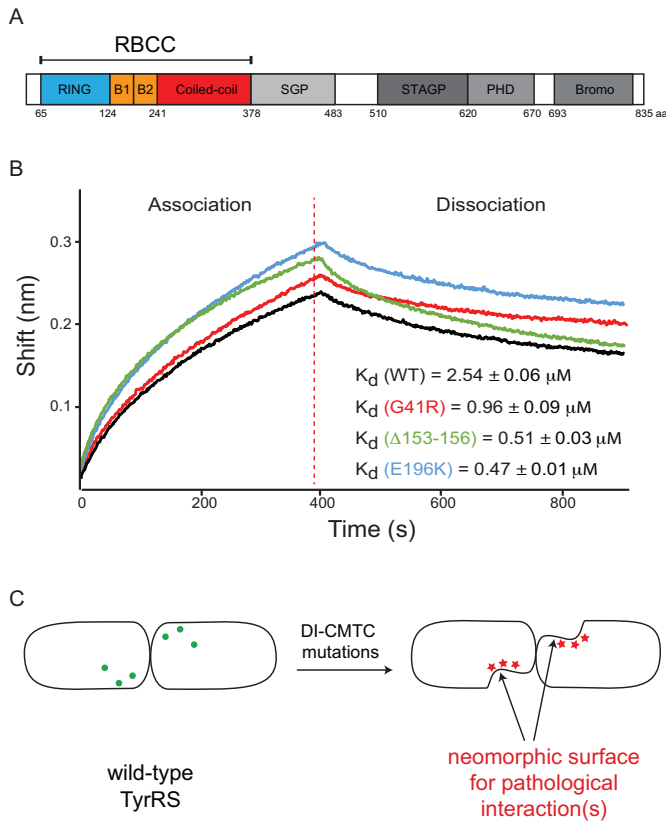
Figure 6. Kinetic analysis of WT TyrRS and TyrRS CMT mutants binding to TRIM28. (**A**) Domain organization of the TRIM28 protein with a highlight on the RBCC domain that was used for the kinetics experiments using Octet red Bio-layer interferometry. (**B**) Binding responses for TyrRS proteins binding to the RBCC domain measured using Octet. A representative data set is shown for each of the four TyrRS protein interactions for which 5 μM of Tag-free RBCC has been injected on an anti-GST biosensor that was coated with GST-tagged TyrRS protein. (**C**) Schematic illustration of the conformational opening of TyrRS induced by CMT-causing mutations, and the generation of a common neomorphic surface involved in potential pathological interactions.

weakening (e.g. L129P) the dimer association (20). However, all CMT2D mutants share conformational opening around the dimerization interface to expose new binding surfaces (20,21), which are correlated with the aberrant GlyRS-Nrp1 interaction that contributes to the neurodegeneration (21). The open conformation seems to be stable, and no aggregation or ubiquitin-positive inclusion was detected in neural tissues of CMT2D mouse models (52). Interestingly, majority of the CMT-causing mutations in tRNA synthetases are located in the catalytic domain (53), and all tRNA synthetases belong to either class I or class II as exemplified by TyrRS and GlyRS, respectively. Although the two classes use completely different molecular architecture for catalysis, both types of architecture may be prone to conformational perturbation, as they were evolved to catalyze an equivalent reaction. Therefore, we suggest that an inherent plasticity, engendering the formation of alternative stable conformations capable of aberrant interactions, may be the common feature for all tRNA synthetase-linked CMT subtypes.

ACCESSION NUMBERS

Structural coordinates have been deposited in the RCSB Protein Data Bank under ID codes 5THH (mini-TyrRS^{E196K}) and 5THL (mini-TyrRS^{G41R}).

SUPPLEMENTARY DATA

Supplementary Data are available at NAR Online.

ACKNOWLEDGEMENTS

FUNDING

REFERENCES

1. Skre,H. (1974) Genetic and clinical aspects of Charcot-Marie-Tooth's disease. *Clin. Genet.*, **6**, 98–118.
2. Rossor,A.M., Tomaselli,P.J. and Reilly,M.M. (2016) Recent advances in the genetic neuropathies. *Curr. Opin. Neurol.*, **29**, 537–548.
3. Antonellis,A., Ellsworth,R.E., Sambuughin,N., Puls,I., Abel,A., Lee-Lin,S.Q., Jordanova,A., Kremensky,I., Christodoulou,K., Middleton,L.T. *et al.* (2003) Glycyl tRNA synthetase mutations in Charcot-Marie-Tooth disease type 2D and distal spinal muscular atrophy type V. *Am. J. Hum. Genet.*, **72**, 1293–1299.
4. Jordanova,A., Irobi,J., Thomas,F.P., Van Dijck,P., Meerschaert,K., Dewil,M., Dierick,I., Jacobs,A., De Vriendt,E., Guergueltcheva,V. *et al.* (2006) Disrupted function and axonal distribution of mutant tyrosyl-tRNA synthetase in dominant intermediate Charcot-Marie-Tooth neuropathy. *Nat. Genet.*, **38**, 197–202.
5. Latour,P., Thauvin-Robinet,C., Baudelet-Mery,C., Soichot,P., Cusin,V., Faivre,L., Locatelli,M.C., Mayencon,M., Sarcey,A., Broussolle,E. *et al.* (2010) A major determinant for binding and aminoacylation of tRNA(Ala) in cytoplasmic Alanyl-tRNA synthetase is mutated in dominant axonal Charcot-Marie-Tooth disease. *Am. J. Hum. Genet.*, **86**, 77–82.
6. Safka Brozkova,D., Deconinck,T., Griffin,L.B., Ferbert,A., Haberlova,J., Mazanec,R., Lassuthova,P., Roth,C., Pilunthanakul,T., Rautenstrauss,B. *et al.* (2015) Loss of function mutations in HARS cause a spectrum of inherited peripheral neuropathies. *Brain*, **138**, 2161–2172.
7. McLaughlin,H.M., Sakaguchi,R., Liu,C., Igarashi,T., Pehlivan,D., Chu,K., Iyer,R., Cruz,P., Cherukuri,P.F., Hansen,N.F. *et al.* (2010) Compound heterozygosity for loss-of-function lysyl-tRNA synthetase mutations in a patient with peripheral neuropathy. *Am. J. Hum. Genet.*, **87**, 560–566.
8. Gonzalez,M., McLaughlin,H., Houlden,H., Guo,M., Yo-Tsen,L., Hadjivassiliou,M., Speziani,F., Yang,X.L., Antonellis,A., Reilly,M.M. *et al.* (2013) Exome sequencing identifies a significant variant in methionyl-tRNA synthetase (MARS) in a family with late-onset CMT2. *J. Neurol. Neurosurg. Psychiatry*, **84**, 1247–1249.
9. Carter,C.W. Jr (1993) Cognition, mechanism, and evolutionary relationships in aminoacyl-tRNA synthetases. *Annu. Rev. Biochem.*, **62**, 715–748.
10. Giege,R. (2006) The early history of tRNA recognition by aminoacyl-tRNA synthetases. *J. Biosci.*, **31**, 477–488.
11. Woese,C.R., Olsen,G.J., Ibba,M. and Soll,D. (2000) Aminoacyl-tRNA synthetases, the genetic code, and the evolutionary process. *Microbiol. Mol. Biol. Rev.*, **64**, 202–236.

12. Xu,X., Shi,Y., Zhang,H.M., Swindell,E.C., Marshall,A.G., Guo,M., Kishi,S. and Yang,X.L. (2012) Unique domain appended to vertebrate tRNA synthetase is essential for vascular development. *Nature Commun.*, **3**, 681.

13. Zhou,Q., Kapoor,M., Guo,M., Belani,R., Xu,X., Kiosses,W.B., Hanan,M., Park,C., Armour,E., Do,M.H. *et al.* (2010) Orthogonal use of a human tRNA synthetase active site to achieve multifunctionality. *Nat. Struct. Mol. Biol.*, **17**, 57–61.

14. Guo,M., Schimmel,P. and Yang,X.L. (2010) Functional expansion of human tRNA synthetases achieved by structural inventions. *FEBS Lett.*, **584**, 434–442.

15. Guo,M., Yang,X.L. and Schimmel,P. (2010) New functions of aminoacyl-tRNA synthetases beyond translation. *Nat. Rev. Mol. Cell. Biol.*, **11**, 668–674.

16. Kim,S., You,S. and Hwang,D. (2011) Aminoacyl-tRNA synthetases and tumorigenesis: more than housekeeping. *Nat. Rev. Cancer*, **11**, 708–718.

17. Sampath,P., Mazumder,B., Seshadri,V., Gerber,C.A., Chavatte,L., Kinter,M., Ting,S.M., Dignam,J.D., Kim,S., Driscoll,D.M. *et al.* (2004) Noncanonical function of glutamyl-prolyl-tRNA synthetase: gene-specific silencing of translation. *Cell*, **119**, 195–208.

18. Motley,W.W., Talbot,K. and Fischbeck,K.H. (2010) GARS axonopathy: not every neuron's cup of tRNA. *Trends Neurosci.*, **33**, 59–66.

19. Storkebaum,E., Leitao-Goncalves,R., Godenschwege,T., Nangle,L., Mejia,M., Bosmans,I., Ooms,T., Jacobs,A., Van Dijck,P., Yang,X.L. *et al.* (2009) Dominant mutations in the tyrosyl-tRNA synthetase gene recapitulate in Drosophila features of human Charcot-Marie-Tooth neuropathy. *Proc. Natl. Acad. Sci. U.S.A.*, **106**, 11782–11787.

20. He,W., Zhang,H.M., Chong,Y.E., Guo,M., Marshall,A.G. and Yang,X.L. (2011) Dispersed disease-causing neomorphic mutations on a single protein promote the same localized conformational opening. *Proc. Natl. Acad. Sci. U.S.A.*, **108**, 12307–12312.

21. He,W., Bai,G., Zhou,H., Wei,N., White,N.M., Lauer,J., Liu,H., Shi,Y., Dumitru,C.D., Lettieri,K. *et al.* (2015) CMT2D neuropathy is linked to the neomorphic binding activity of glycyl-tRNA synthetase. *Nature*, **526**, 710–714.

22. Hyun,Y.S., Park,H.J., Heo,S.H., Yoon,B.R., Nam,S.H., Kim,S.B., Park,C.I., Choi,B.O. and Chung,K.W. (2014) Rare variants in methionyl- and tyrosyl-tRNA synthetase genes in late-onset autosomal dominant Charcot-Marie-Tooth neuropathy. *Clin. Genet.*, **86**, 592–594.

23. Gonzaga-Jauregui,C., Harel,T., Gambin,T., Kousi,M., Griffin,L.B., Francescatto,L., Ozes,B., Karaca,E., Jhangiani,S.N., Bainbridge,M.N. *et al.* (2015) Exome sequence analysis suggests that genetic burden contributes to phenotypic variability and complex neuropathy. *Cell Rep.*, **12**, 1169–1183.

24. Froelich,C.A. and First,E.A. (2011) Dominant Intermediate Charcot-Marie-Tooth disorder is not due to a catalytic defect in tyrosyl-tRNA synthetase. *Biochemistry*, **50**, 7132–7145.

25. Niehues,S., Bussmann,J., Steffes,G., Erdmann,I., Kohrer,C., Sun,L., Wagner,M., Schafer,K., Wang,G., Koerdt,S.N. *et al.* (2015) Impaired protein translation in Drosophila models for Charcot-Marie-Tooth neuropathy caused by mutant tRNA synthetases. *Nat. Commun.*, **6**, 7520.

26. Whitmore,L. and Wallace,B.A. (2008) Protein secondary structure analyses from circular dichroism spectroscopy: methods and reference databases. *Biopolymers*, **89**, 392–400.

27. Yang,X.L., Skene,R.J., McRee,D.E. and Schimmel,P. (2002) Crystal structure of a human aminoacyl-tRNA synthetase cytokine. *Proc. Natl. Acad. Sci. U.S.A.*, **99**, 15369–15374.

28. Konarev,P.V., Volkov,V.V., Sokolova,A.V., Koch,M.H.J. and Svergun,D.I. (2003) PRIMUS: a Windows PC-based system for small-angle scattering data analysis. *J. Appl. Crystallogr.*, **36**, 1277–1282.

29. Svergun,D.I. and Koch,M.H.J. (2003) Small-angle scattering studies of biological macromolecules in solution. *Rep. Prog. Phys.*, **66**, 1735–1782.

30. Franke,D. and Svergun,D.I. (2009) DAMMIF, a program for rapid ab-initio shape determination in small-angle scattering. *J. Appl. Crystallogr.*, **42**, 342–346.

31. Volkov,V.V. and Svergun,D.I. (2003) Uniqueness of ab initio shape determination in small-angle scattering. *J. Appl. Crystallogr.*, **36**, 860–864.

32. Li,S., Tsalkova,T., White,M.A., Mei,F.C., Liu,T., Wang,D., Woods,V.L. Jr and Cheng,X. (2011) Mechanism of intracellular cAMP sensor Epac2 activation: cAMP-induced conformational changes identified by amide hydrogen/deuterium exchange mass spectrometry (DXMS). *J. Biol. Chem.*, **286**, 17889–17897.

33. Mendillo,M.L., Hargreaves,V.V., Jamison,J.W., Mo,A.O., Li,S., Putnam,C.D., Woods,V.L. Jr and Kolodner,R.D. (2009) A conserved MutS homolog connector domain interface interacts with MutL homologs. *Proc. Natl. Acad. Sci. U.S.A.*, **106**, 22223–22228.

34. Walters,B.T., Ricciuti,A., Mayne,L. and Englander,S.W. (2012) Minimizing back exchange in the hydrogen exchange-mass spectrometry experiment. *J. Am. Soc. Mass Spectrom.*, **23**, 2132–2139.

35. Marsh,J.J., Guan,H.S., Li,S., Chiles,P.G., Tran,D. and Morris,T.A. (2013) Structural insights into fibrinogen dynamics using amide hydrogen/deuterium exchange mass spectrometry. *Biochemistry*, **52**, 5491–5502.

36. Zhang,Z. and Smith,D.L. (1993) Determination of amide hydrogen exchange by mass spectrometry: a new tool for protein structure elucidation. *Protein Sci.*, **2**, 522–531.

37. Langer,A., Hampel,P.A., Kaiser,W., Knezevic,J., Welte,T., Villa,V., Maruyama,M., Svejda,M., Jahner,S., Fischer,F. *et al.* (2013) Protein analysis by time-resolved measurements with an electro-switchable DNA chip. *Nat. Commun.*, **4**, 2099.

38. Yaremchuk,A., Kriklivyi,I., Tukalo,M. and Cusack,S. (2002) Class I tyrosyl-tRNA synthetase has a class II mode of cognate tRNA recognition. *EMBO J.*, **21**, 3829–3840.

39. Kleeman,T.A., Wei,D., Simpson,K.L. and First,E.A. (1997) Human tyrosyl-tRNA synthetase shares amino acid sequence homology with a putative cytokine. *J. Biol. Chem.*, **272**, 14420–14425.

40. Wakasugi,K. and Schimmel,P. (1999) Two distinct cytokines released from a human aminoacyl-tRNA synthetase. *Science*, **284**, 147–151.

41. Yang,X.L., Liu,J., Skene,R.J., McRee,D.E. and Schimmel,P. (2003) Crystal structure of an EMAP-II-like cytokine released from a human tRNA synthetase. *Helv. Chim. Acta.*, **86**, 1246–1257.

42. Lee,P.S., Zhang,H.M., Marshall,A.G., Yang,X.L. and Schimmel,P. (2012) Uncovering of a short internal peptide activates a tRNA synthetase procytokine. *J. Biol. Chem.*, **287**, 20504–20508.

43. Langer,A., Kaiser,W., Svejda,M., Schwertler,P. and Rant,U. (2014) Molecular dynamics of DNA-protein conjugates on electrified surfaces: solutions to the drift-diffusion equation. *J. Phys. Chem. B*, **118**, 597–607.

44. Fu,G., Xu,T., Shi,Y., Wei,N. and Yang,X.L. (2012) tRNA-controlled nuclear import of a human tRNA synthetase. *J. Biol. Chem.*, **287**, 9330–9334.

45. Wei,N., Shi,Y., Truong,L.N., Fisch,K.M., Xu,T., Gardiner,E., Fu,G., Hsu,Y.S., Kishi,S., Su,A.I. *et al.* (2014) Oxidative stress diverts tRNA synthetase to nucleus for protection against DNA damage. *Mol. Cell*, **56**, 323–332.

46. Soto,C. (2003) Unfolding the role of protein misfolding in neurodegenerative diseases. *Nat. Rev. Neurosci.*, **4**, 49–60.

47. Knowles,T.P., Vendruscolo,M. and Dobson,C.M. (2014) The amyloid state and its association with protein misfolding diseases. *Nat. Rev. Mol. Cell. Biol.*, **15**, 384–396.

48. Stefanis,L. (2012) alpha-Synuclein in Parkinson's disease. *Cold Spring Harb. Perspect. Med.*, **2**, a009399.

49. Valastyan,J.S. and Lindquist,S. (2014) Mechanisms of protein-folding diseases at a glance. *Dis. Model. Mech.*, **7**, 9–14.

50. Fandrich,M., Fletcher,M.A. and Dobson,C.M. (2001) Amyloid fibrils from muscle myoglobin. *Nature*, **410**, 165–166.

51. Nangle,L.A., Zhang,W., Xie,W., Yang,X.L. and Schimmel,P. (2007) Charcot-Marie-Tooth disease-associated mutant tRNA synthetases linked to altered dimer interface and neurite distribution defect. *Proc. Natl. Acad. Sci. U.S.A.*, **104**, 11239–11244.

52. Stum,M., McLaughlin,H.M., Kleinbrink,E.L., Miers,K.E., Ackerman,S.L., Seburn,K.L., Antonellis,A. and Burgess,R.W. (2011) An assessment of mechanisms underlying peripheral axonal degeneration caused by aminoacyl-tRNA synthetase mutations. *Mol. Cell. Neurosci.*, **46**, 432–443.

53. Storkebaum,E. (2016) Peripheral neuropathy via mutant tRNA synthetases: Inhibition of protein translation provides a possible explanation. *Bioessays*, **38**, 818–829.